ADVANCED SCIENCE Open Access
www.advancedscience.com

3D Micropatterned Traction Force Microscopy: A Technique to Control 3D Cell Shape While Measuring Cell-Substrate Force Transmission

Laura M. Faure, Manuel Gómez-González, Ona Baguer, Jordi Comelles, Elena Martínez, Marino Arroyo, Xavier Trepat,* and Pere Roca-Cusachs**

Cell shape and function are intimately linked, in a way that is mediated by the forces exerted between cells and their environment. The relationship between cell shape and forces has been extensively studied for cells seeded on flat 2D substrates, but not for cells in more physiological 3D settings. Here, a technique called 3D micropatterned traction force microscopy (3D-μTFM) to confine cells in 3D wells of defined shape, while simultaneously measuring the forces transmitted between cells and their microenvironment is demonstrated. This technique is based on the 3D micropatterning of polyacrylamide wells and on the calculation of 3D traction force from their deformation. With 3D-μTFM, it is shown that MCF10A breast epithelial cells exert defined, reproducible patterns of forces on their microenvironment, which can be both contractile and extensile. Cells switch from a global contractile to extensile behavior as their volume is reduced are further shown. The technique enables the quantitative study of cell mechanobiology with full access to 3D cellular forces while having accurate control over cell morphology and the mechanical conditions of the microenvironment.

1. Introduction

Cells within tissues exert forces on each other and on their microenvironment, modifying their shape and that of the tissue. This mechanical control of cell shape regulates developmental processes from gastrulation to organogenesis, disease progression, and aging.[1–3] Thus, the relationship between cell shape and cell mechanical forces is of major importance and has been extensively studied on 2D surfaces. By combining cell micropatterning with force-measuring techniques such as traction force microscopy (TFM) or micropillars, researchers established a correlation between cell spreading area and the forces cells generate.[4–7] However, cells spreading on 2D surfaces do not adequately model the shape found in several physiological conditions, highlighting the need for a system to control cell shape in three dimensions (3D) while measuring cell mechanical forces.

TFM, based on measuring the displacement of fiducial markers embedded in an elastic substrate, is one of the main techniques used to measure how cells exert forces on their surroundings. This technique was originally developed to measure 2D forces generated by single cells on flat surfaces but has since been extended to measure 3D forces produced by single cells,[8,9] cell monolayers,[10] and single cells or groups

L. M. Faure, M. Gómez-González, O. Baguer, J. Comelles, E. Martínez, M. Arroyo, X. Trepat, P. Roca-Cusachs
Institute for Bioengineering of Catalonia (IBEC)
Barcelona Institute of Science and Technology (BIST)
C. Baldiri Reixac 10-12, Barcelona 08028, Spain
E-mail: lfaure@ibecbarcelona.eu; xtrepat@ibecbarcelona.eu; proca@ibecbarcelona.eu

O. Baguer, X. Trepat, P. Roca-Cusachs
Department of Biomedical Sciences
University of Barcelona
C. Casanova 143, Barcelona 08034, Spain

J. Comelles, E. Martínez
Department of Electronics and Biomedical Engineering
University of Barcelona
C. Martí Franquès 1, Barcelona 08028, Spain

E. Martínez, X. Trepat
Centro de Investigación Biomédica en Red en Bioingeniería
Biomateriales y Nanomedicina (CIBER-BBN)
Avenida Monforte de Lemos 3-5, Madrid 28029, Spain

M. Arroyo
Laboratori de Càlcul Numèric (LaCàN)
Universitat Politècnica de Catalunya (UPC)
Jordi Girona 1-3, Barcelona 08036, Spain

M. Arroyo
Institut de Matemàtiques de la UPC–BarcelonaTech (IMTech)
Pau Gargallo 14, Barcelona 08028, Spain

M. Arroyo
Centre Internacional de Mètodes Numèrics en Enginyeria (CIMNE)
Gran Capità S/N, Barcelona 08034, Spain

X. Trepat
Institució Catalana de Recerca i Estudis Avançats (ICREA)
Lluis Companys 23, Barcelona 08010, Spain

The ORCID identification number(s) for the author(s) of this article can be found under https://doi.org/10.1002/advs.202406932

DOI: 10.1002/advs.202406932

of cells embedded inside hydrogels in 3D.[11–13] In parallel, microniche techniques have been developed to control cell shape in 3D.[14–16] However, none of the existing systems allow for the 3D control of cell shape while measuring cell forces, even though this relationship is fundamental in vivo.[10] In this work, we present a technique to compute traction forces generated by single cells in 3D micro-structures, 3D micropatterned traction force microscopy (3D-μTFM), and we apply it to study the relationship between cell shape and force in 3D. We show that epithelial cells display specific force patterns depending on their volume. While larger cells exert mostly contractile forces consistently with what has been described on 2D substrates, smaller cells generate extensile forces on their microenvironment through their actin cytoskeleton.

2. Results

2.1. Measuring 3D Forces While Controlling Cell Morphology

We used microfabrication techniques,[16,17] to develop a structured hydrogel to control cell morphology while enabling the measurement of 3D traction forces. As the material for our hydrogels, we chose polyacrylamide due to its linear elastic behavior, transparency, tuneability, and widespread use in TFM on flat surfaces,[18–20] (**Figure 1**). By polymerizing gels in contact with a poly(dimethylsiloxane) (PDMS) mold containing pillars, we generated wells in our gels with a size comparable to that of single cells. To tune cell size, we used pillars of 9 μm in height and either 15 μm or 19 μm in diameter. Because of gel swelling after polymerization, the resulting well dimensions were slightly different than the molds: 11–12 μm in height, and 10–11 μm or 14–16 μm in diameter, respectively. We refer to them as small and large wells, with volumes of 1060 $\mu m^3 \pm 10\%$ and 1930 $\mu m^3 \pm 9\%$ (mean ± standard deviation). Smaller and larger wells than these were also prepared, but our cellular model (MCF10A breast epithelial cells) either did not fit in very small wells or did not completely fill very large wells (Figure S1, Supporting Information). Thus, these wells were discarded in further experiments. Fluorescent microbeads were added to the gel mixture as fiducial markers for measuring gel deformations. Beads accumulated near the free surfaces of the gel during polymerization. This accumulation was beneficial, as the distribution of beads on a thin layer enhances the accuracy of surface displacement measurements compared to a uniform, bulk bead distribution. Finally, we provided cell ligands to the wells by covalent binding of fibronectin to the gel surface.

Having obtained control over cell shape, we proceeded to image our system to compute 3D traction forces. To achieve an optimal compromise between spatial and temporal resolution, we used a fast airy-scan confocal microscope (Carl Zeiss Ltd.). Following a workflow analogous to 2D-TFM (Figure 1C) we first set up a particle image velocimetry (3D PIV) algorithm to measure the 3D displacements of the fluorescent beads. Our 3D PIV compares a 3D stack image of the deformed gel with a 3D stack of the relaxed state, providing a 3D deformation map. Only displacements of the surface of the gel, including the top surface, the well wall, and the well bottom, were needed for our calculation. Then, we developed an inverse method to compute the 3D tractions through finite element modeling (FEM), imposing the measured displacement on a geometrical model of our wells. For each well size, a model was created as a cylindrical cavity of the same radius and depth as the imaged well. The model was meshed, and the mesh nodes of the upper surface were aligned with the 3D stack image of the gel relaxed state. The 3D tractions at the gel-cell interface were then obtained by solving an inverse FEM problem minimizing the discrepancy between computational and measured 3D displacements, introducing mechanical equilibrium as constraints in the optimization (Note S1, Supporting Information).

To represent the computed tractions, we took advantage of the cylindrical symmetry of the wells. We unfolded the traction fields exerted on the lateral wall and represented them as a rectangle, whereas we represented the traction fields exerted on the well bottom as a disk (Figure 1D). For better visualization and comparison of traction results, we decomposed the total tractions in normal, vertical, and circumferential traction maps for the wall (T_n-wall, T_v-wall, and T_c-wall, respectively) and normal, radial, and circumferential traction maps for the bottom (T_n-bottom, T_r-bottom, and T_c-bottom, respectively) (Figure 1D). From these maps, we average the traction components along the well circumference and represent those averages as a function of the radial distance from the center of the well (for the bottom surface) and as a function of the vertical distance from the well top (for the lateral wall).

2.2. Characterization of the System

To estimate noise levels and assess the effect of gel swelling during medium changes, we first carried out our experimental protocol using empty wells (Figure S2, Supporting Information). Wall tractions showed values generally below 100 Pa, and no distinct pattern of forces on the maps except for peaks of 250 Pa at the top edge of T_n-wall. In bottom tractions, peaks of 250 Pa were also found at the edge. In both the walls and bottom of wells, edges are where we expected the largest discretization errors of the experimental well due to inaccuracies in precisely determining well shape (see Experimental Section). T_r-bottom and T_c-bottom maps showed dipole patterns with values around 500 Pa, associated with residual misalignment of the images (Figure S2Q–X, Supporting Information). Except for the edge effects in the wall and bottom, all traction noises largely canceled out when computing average profiles along the wall height, or the bottom radius (Figure S2, Supporting Information). Comparing these average noise profiles to those of real cells (described below), signal-to-noise ratios were above 9.

Another potential source of noise comes from the cells themselves. Cells are known to induce lensing effects in microscopy images due to their shape, their nucleus, and to differences in refractive index between themselves (≈1.36) and their surrounding media (≈1.34).[21] These effects, in the order of hundreds of nanometers, have been shown to create aberrations in the measurement of forces generated by cells placed on 2D micropillars.[21] and are generally more complex in 3D settings. One of the strengths of our method is that, because our wells have simple and reproducible geometries, we can theoretically estimate and experimentally measure the displacement introduced by the difference in refraction index. We were thus able to correct

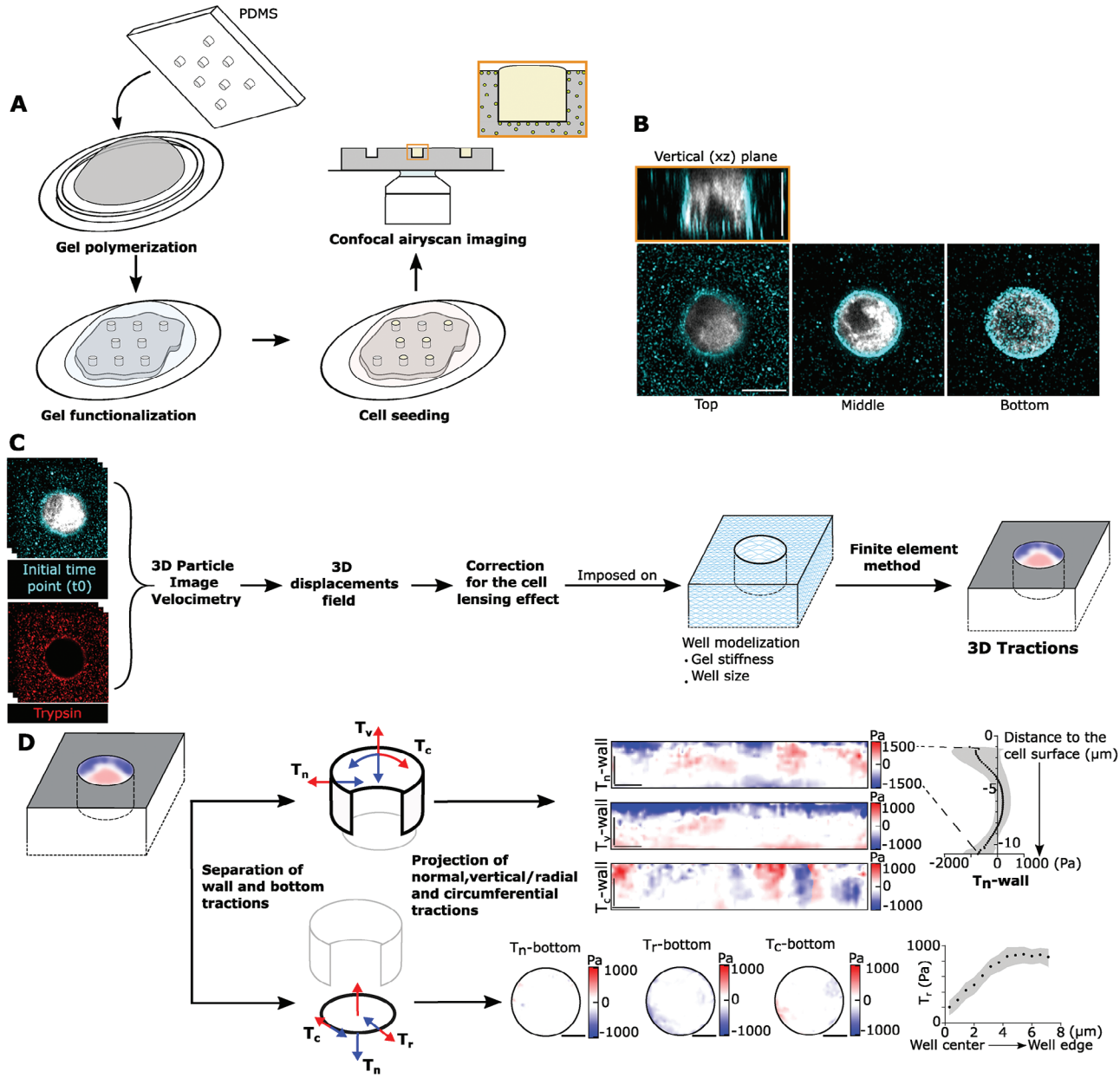

Figure 1. Workflow to measure 3D forces generated by cells of controlled morphologies. A) Production of the experimental set-up. B) Example of a cell (in white, labeled with CellTracker) in a well, fluorescent beads are shown in cyan. Scale bar: 10 μm. C) Pipeline analysis. For better visualization of the bead displacements generated by cells, the images of the beads in the initial and relaxed positions (before/after trypsinization) are artificially displayed in cyan and red, respectively. D) From 3D tractions in the wells, maps of normal, vertical, and circumferential tractions to the wall (T_n-wall, T_v-wall, and T_c-wall, respectively) were calculated, and maps of normal, radial, and circumferential tractions to the bottom of the well (T_n-bottom, T_r-bottom, and T_c-bottom, respectively) were computed. From these maps, mean profiles of tractions were obtained and represented along the *z*-axis for the wall of the well or radially for the bottom of the well. See arrow colors for directions of positive/negative tractions in each case. Scale bar: 10 μm.

it before calculating 3D tractions through FEM (Figure 1C; Note S2, Figures S3–S5 Supporting Information). After this correction, we measured traction forces in a condition where they should not be present, trypsinized cells (Figure S5, Supporting Information). As it considers all potential sources, we took this measurement as a more complete quantification of noise, and we used it for the rest of the manuscript. Using this quantification of noise, average traction patterns showed signal-to-noise levels above 3.5, except in specific conditions discussed below.

2.3. Cells Exert Contractile Forces When Placed in a Large PAA Well

When cells are adhered on 2D surfaces,[18–20] or embedded in 3D gels,[11,12] they are well known to exert contractile forces. We thus tested if cells confined in cylindrical wells display similar mechanical behavior. To do so, we seeded MCF10A in our large wells, and measured traction forces. Forces normal to the wall (T_n-wall) showed a characteristic pattern that varies along the

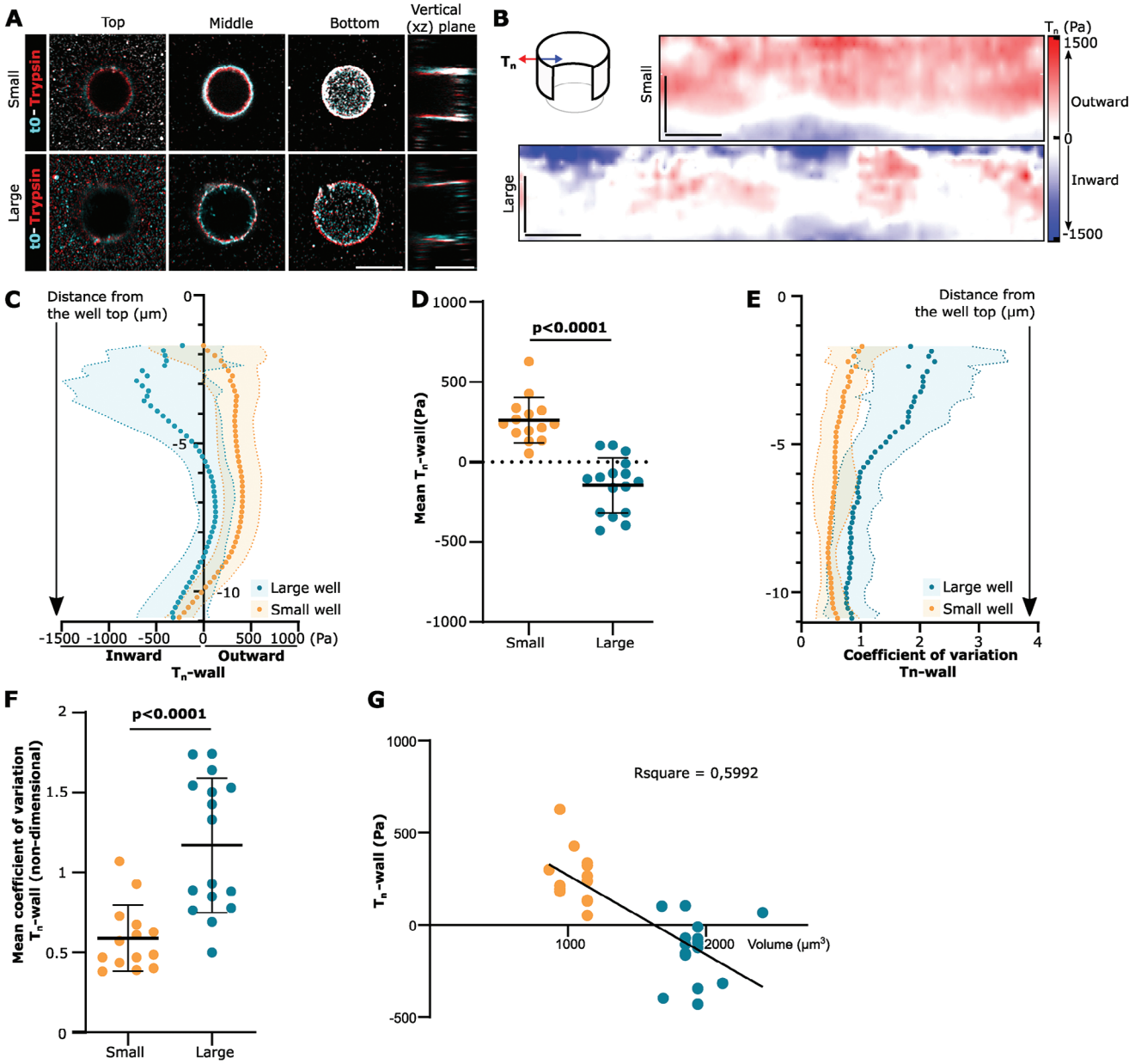

Figure 2. Cells push or pull depending on their volume. A) Superposition of bead localization before (cyan) and after (red) trypsinization of example cells on small/large wells. Three xy planes of the stacks are shown (Top, Middle, and Bottom of the well), and a vertical plane (xz) of the same stacks. Scale bars: 10 µm. B) Corresponding T_n-wall maps. Scale bars: 5 µm. C) Average T_n-wall profiles along the *z*-axis. D) T_n-wall mean. $p < 0.0001$, Mann–Whitney test. E) Coefficient of variation of T_n-wall profiles along the *z*-axis. F) Mean of the coefficient of variation of T_n-wall profiles. $p < 0.0001$, unpaired *t*-test. G) Mean T_n-wall as a function of cell volume (µm^3). Data are mean ± standard deviation, $n = 14$ and $n = 16$ cells for the small and the large well conditions, respectively, from at least three independent experiments.

z-axis. From top to bottom, forces are directed inward, outward, and inward again with a higher magnitude for inward-directed forces (average maximum at 700 Pa), than for outward-directed forces (average maximum at 150 Pa, **Figure** 2A–C). Vertical forces along the wall (T_v-wall) show downward-directed forces at the top of the wall (1000 Pa in average) and upward-directed forces at the bottom (300 Pa in average, **Figure** 3A–C). Thus, cells contract the walls, pulling the wall top and bottom toward the center. Radial bottom tractions (T_r-bottom) showed a similar pattern of contractile forces, where cells pull the bottom edge toward the center (700 Pa on average, Figure 3D–F).

Normal and circumferential forces to the bottom of the well (T_n-bottom and T_c-bottom, respectively) are lower, with traction profiles below 100 Pa (Figure S6D–I, Supporting Information). Finally, circumferential forces along the wall (T_c-wall) can reach 500 Pa but do not present a preferential directionality, as shown by mean profiles lower than 100 Pa (Figure S6A–C, Supporting Information). Average forces in these directions thus

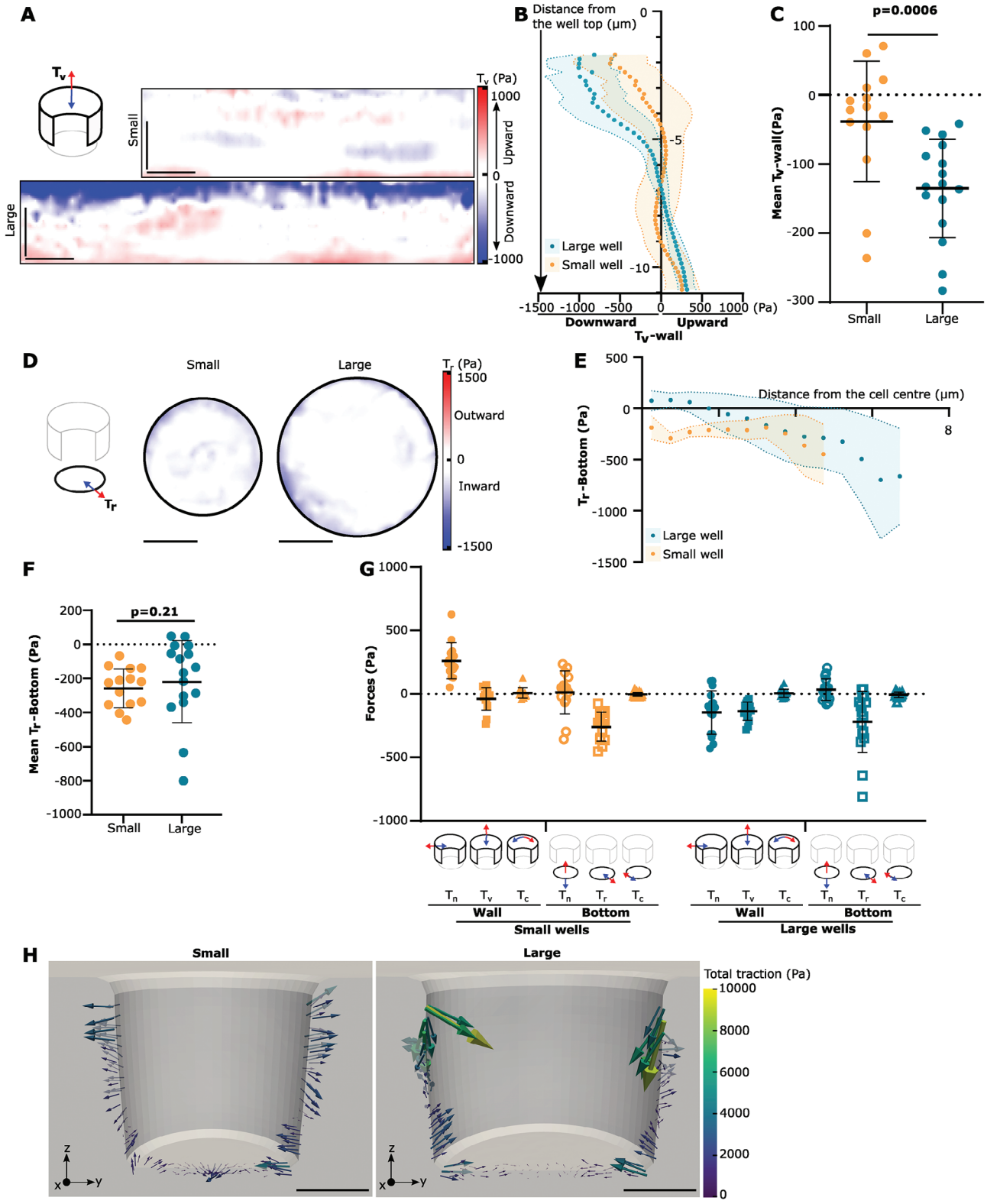

Figure 3. Characterization of cell forces in different directions in 3D. A) Example T_v-wall maps. Scale bars: 5 µm. B) Average T_v-wall profiles along the *z*-axis. C) T_v-wall mean. $p = 0.0006$, Mann–Whitney test. D) Example T_r-bottom maps. Scale bars: 5 µm. E) Average radial profiles of the T_r-bottom tractions. F) T_r-bottom mean. $p = 0.21$, Mann–Whitney test. G) Comparison of mean forces for each well surface (wall/bottom) and each well size (small/large). H) Traction forces of a representative vertical cut from the small and large well (Data displayed with Paraview). Scale bar: 5 µm. Data are mean ± standard deviation, $n = 14$ and $n = 16$ cells for the small and the large well conditions, respectively, from at least three independent experiments.

essentially measure noise and are only 30% higher than noise levels (Figure S6, Supporting Information). Moreover, their positioning does not correlate with any of the previous patterns from the T_n-wall or the T_v-wall.

To extend the data beyond one cell type, we also measured forces in MCF7 breast cancer cells, observing similar trends. Indeed, the largest forces were exerted normal to the well wall (T_n-wall), both contractile and extensile, vertically along the wall (T_v-wall), pulling downward at the top and upward at the bottom, and in the radial direction along the wall bottom (T_r-bottom), contractile toward the cell center (Figure S7, Supporting information). As an interesting difference, T_n-wall forces in MCF7 cells were extensile mostly at the wall top, in contrast with MCF10As (which were extensile mostly at the wall center). We note that in MCF7 cells effects of well volume (which we discuss below for MCF10A) could not be assessed, as cells generally did not conform to the shape of large wells, potentially due to elevated cortical stiffness.

In conclusion, the directions where the largest forces were applied were normal to the wall (either contractile or extensile) and radial along the bottom (Figure 3G). In this way, MCF10A cells placed in the large wells present a characteristic traction pattern consisting of an apical and a basal ring of contractility which pull the well edges toward the cell center (Figure 3H).

2.4. Cell Mechanical Behavior Depends on Cell Volume

Next, we compared the large wells described above (volume of 1930 $\mu m^3 \pm 9\%$, mean ± standard deviation) to smaller wells (volume of 1060 $\mu m^3 \pm 10\%$, mean ± standard deviation). Forces normal to the wall (T_n-wall) in cells seeded in small wells pointed outward along the top two-thirds of the wells (Figure 2A–C). Overall, the average of the T_n-wall was positive for small wells but negative for large wells, meaning that cells in small wells exert extensile forces and not contractile forces (Figure 2D). Interestingly, T_n-wall forces were also more homogeneous in small wells, as quantified by a lower coefficient of variation (standard deviation divided by the mean, Figure 2E,F). This shows that cells in small wells lose the polar configuration with contractile peaks at the bottom and top, and rather exert a more homogeneous outward, extensile force. Taking advantage of the variability of volumes of each individual well given by the fabrication procedure, we also plotted T_n-wall forces as a function of cell volume. The results showed a good correlation, with an estimated switch from contractile to extensile forces at around 1600 μm^3 (Figure 2G).

Apart from T_n-wall, other force patterns in small wells showed changes in their magnitude with respect to large wells, but not in their orientation. Cells placed in small wells still exert inward-directed forces at the bottom of the well but of slightly lower magnitude (500 Pa) than cells placed in large wells (700 Pa, Figure 3D–F). This is comparable to what was shown for cells placed on 2D patterns of different sizes.[4,5] Cells placed in the smaller wells also exert downward-directed forces at the top of the well and upward-directed forces at the bottom of the well, but of lower magnitude than for the large wells, with maximum values below 500 Pa (Figure 3A,B). As for large wells, T_c-wall and T_c-bottom maps display tractions generally below 400 and 300 Pa, respectively, and no preferred directionality (Figure S6, Supporting Information). To conclude, confining cells to a smaller volume in the xy plane reduced overall force generation and changed cell mechanical behavior from contractile to extensile (Figure 3H).

As an additional analysis of cell shape, we measured cells in shallower wells with lower walls (5–6 μm in height, 22–24 μm in diameter, 2360 ± 8% in volume). In these conditions, pushing forces along the walls were eliminated, leaving only contractile forces (Figure S8, Supporting Information). This provides a nice transition between 3D and 2D shapes: a cell inside a shallow well has a shape closer to that found in 2D, where most of the cell-substrate contact area is along the horizontal surface below the cell. Accordingly, these cells show a contractile behavior, similar to that found in 2D.

2.5. Contractile Behavior in Large Wells Depends on Actin and Myosin Activity, While Extensile Behavior in Small Wells Requires Actin Polymerization

Cell generation of contractile forces has been widely studied and is mediated by the actomyosin cytoskeleton.[16,19,20] To assess the roles of both actin and myosin in the mechanical patterns observed in both small and large wells, we inhibited both actin polymerization with 0.5 μM latrunculin A (LatA), and myosin contractility with 25 μM blebbistatin (Bleb), using concentrations previously shown to effectively inhibit actin or myosin in our cell system.[20,22] To evaluate the effect of the drugs, we used our 3D-μTFM pipeline to compare the conditions before and after their addition (**Figure 4**).

We focus on T_n-wall as it shows the highest forces and most relevant changes with cell size. In large wells, T_n-wall maps are strongly affected by both latrunculin A and blebbistatin (Figure 4B). The maps and traction profiles in the latrunculin A and blebbistatin conditions show very low forces, with only residual traction at the top edge (Figure 4B–D) and a 70–75% reduction in tractions with respect to control conditions (Figure 4E). Besides, we observed similar trends in T_v-wall and T_r-bottom (Figure S9A-H, Supporting Information). In conclusion, and consistent with what has been shown on 2D surfaces, the contractile activity we observe in the large wells is due to the actomyosin cytoskeleton. Moreover, it is worth noticing that the inhibition of myosin contractility through the addition of blebbistatin is sufficient to flatten both inward-directed forces (contractile) and outward-directed forces (extensile) in the T_n-wall (Figure 4D). Likely, the forces generated by the contractile top and bottom rings are strong enough to cause hydrostatic pressure pushing on the central part of the wall of the well.

In contrast to what we observe in large wells, the addition of latrunculin A or blebbistatin leads to different results in small wells. Latrunculin A reduced T_n-wall forces almost completely (97% for the mean). However, blebbistatin induced a much milder trend toward force reduction in T_n-wall forces (55% for the mean) which was not significant (Figure 4F–I). Similar trends are observed for T_r-bottom (Figure S9M–P, Supporting Information) while neither blebbistatin nor latrunculin A induced a significant change on the T_v-wall (Figure S9I–L, Supporting Information) which could be explained by the low force values already observed in case of the control. This indicates that actin polymerization but not myosin contractility generates most of the extensile forces exerted by cells placed in small wells (Figure 4J).

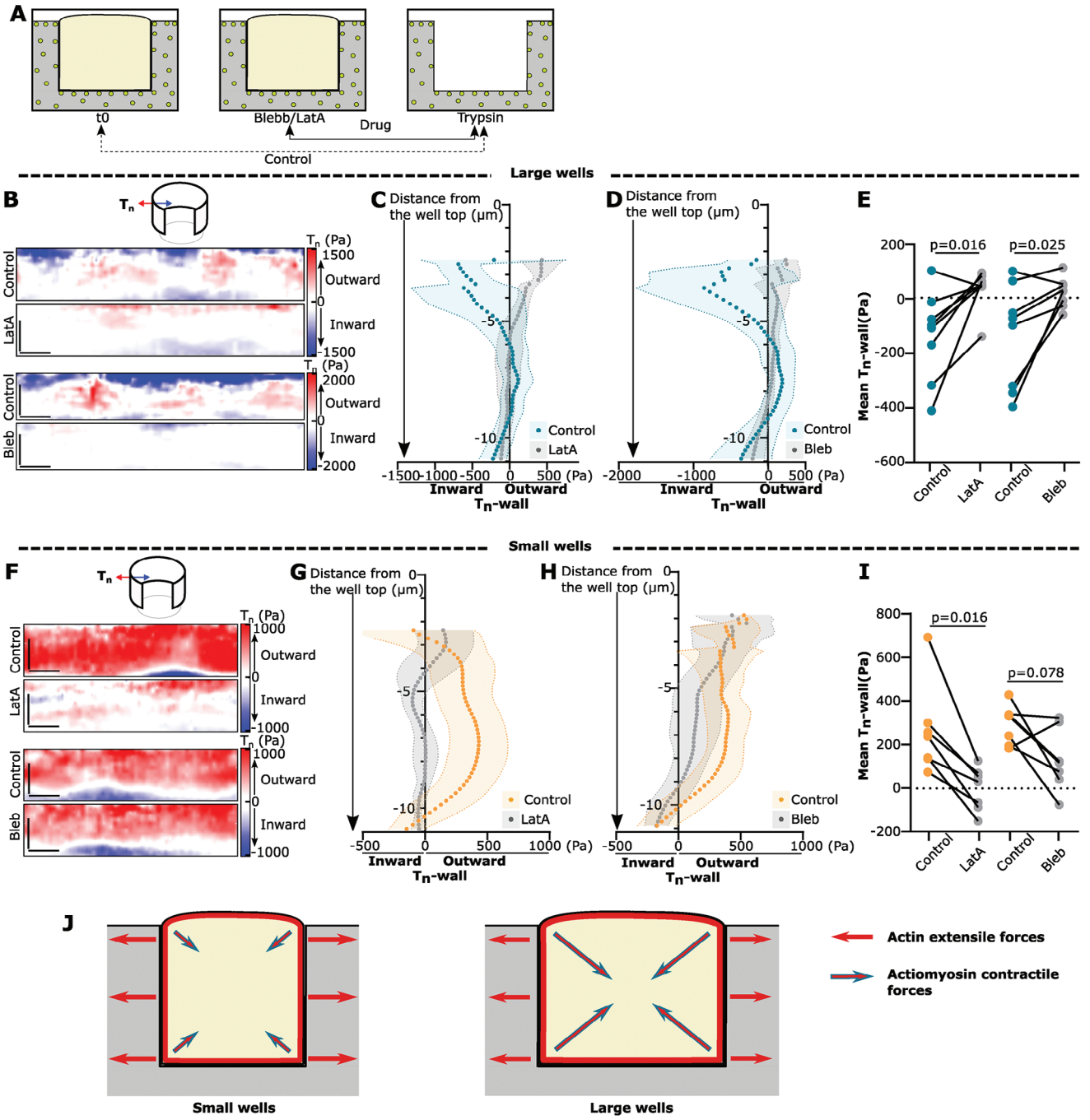

Figure 4. Contractile behavior in large wells depends on actin and myosin activity, while extensile behavior in small wells requires actin polymerization. A) Schematic of the experimental set-up, bead positions in gels before any treatment (Control) or after the addition of blebbistatin (Bleb) or latrunculin A (LatA) are compared to bead positions after complete cell removal by trypsinization. B,F) Example T_n-wall maps comparing the blebbistatin/latrunculin A condition to the control for large B), and small F) wells. Scale bars: 5 μm. C,D,G,H) Average T_n-wall profiles along the *z*-axis for large C,D), and small G,H) wells. Data are mean ± standard deviation. (E, I) Example T_n-wall means for large E), and small I) wells. Mean paired data are represented as connected. For large wells, Control/LatA: $p = 0.0016$, Wilcoxon matched-pairs signed rank test; Control/Bleb: $p = 0.025$, paired *t*-test. For small wells, Control/ LatA: $p = 0.016$, Wilcoxon matched-pairs signed rank test; Control/Bleb: $p = 0.078$, Wilcoxon matched-pairs signed rank test. $n = 8$ cells for each large well condition, $n = 7$ for each small well condition, from at least three independent experiments. J) Cartoon representative of the forces applied. Extensile and contractile forces can be measured in both small and large wells, but extensile forces dominate in small wells, whereas contractile forces dominate in large wells.

3. Conclusion

In this study, we present a structured hydrogel system that allows for the measurement of forces generated by single cells of defined morphologies in 3D. 3D-TFM was demonstrated over 10 years ago,[8,9,11] and has been refined since.[12,13,23] However, previous approaches did not control cell shape, and one of their difficulties lies precisely in the proper detection of the cell contour, which heavily influences traction results and can create cell lensing effects. By using wells of defined shape, we not only removed this complexity in traction computation, but we also obtained very regular maps of traction, where the lensing effect was corrected. This allowed us to easily recognize and compare force patterns, such as the two contractile rings present in the large wells. Another issue in previous 3D-TFM approaches arose from the use of non-linear, degradable, or viscoelastic gels, which required important approximations to calculate forces.[12] We chose to prevent this by using polyacrylamide hydrogels, which are linear elastic, with known elastic properties. Finally, we note that confocal images do not present the same resolution in x/y and z, meaning that errors in displacements are larger along the *z*-axis. This generates asymmetry in the traction noise. By separating the total tractions into T_n-wall, T_v-wall, T_c-wall, T_n-bottom, T_r-bottom, and T_c-bottom we compare tractions that are more influenced by either the xy or z displacements, thus isolating the different components. Another solution would be to use light-sheet microscopes to image the set-ups, since it produces images with isotropic resolution, although lensing effects might be more severe.

The ability of cells to exert both pulling and pushing forces has been well described, although measuring pulling forces has proven to be easier. Pushing forces, exerted by extensile cellular structures such as lamellipodia, filopodia, and podosomes,[24–27] have typically been measured using low throughput techniques such as Atomic Force Microscopy (AFM), optical or magnetic tweezers, and glass fiber deflection. For example, AFM has been used to measure extensile forces by keratinocyte lamellipodia,[24] or by macrophage podosomes,[26,27] of the order of 10 nN. Recent findings on amoeboid migration have also highlighted the importance of protrusive forces at the cell leading edge, but related forces have not been measured, due to the complexity of the system, for cells fully embedded in 3D matrices.[28] In this study, we present a novel method that allowed us to uncover a new mechanical behavior: an extensile force consistently applied over the cell diameter when cells are confined in a plane. We estimate that this force is around 90nN, which is significantly higher than what has been observed for pushing forces until now. This difference could be explained by the large area over which this pushing force is applied (500 μm^2) when compared to lamellipodia (0.6 μm^2 in,[24]) or podosomes (1–12 μm^2).

The ability of our system to measure extensile forces allowed us to determine that diminishing cell diameter from 14 µm to 11 µm is sufficient to switch cell mechanical behavior from contractile to extensile. Forcing cells into smaller volumes may increase protein concentration, and this could affect actin organization. In turn, contractile forces exerted by myosin II motors depend on actin organization, specifically on the length of actin filaments,[29] the state of these filaments (bundled or branched,[30,31]), and the ability of myosin II to enter the actin mesh.[29] Thus, we hypothesize that such effects on actomyosin organization could explain the observed mechanical effect of cell volume. Consistently with this hypothesis, the total measured actin content from immunostainings was not affected by cell volume, suggesting a change in concentration (Figure S10, Supporting Information). Such a change could also explain the difference in the lensing effect detected between cells placed in small or large wells.[33] On top of specific effects on actomyosin, changes in cell volume may also affect cell pressure, which could also regulate cell mechanical forces.[34] Further studies are needed to verify this hypothesis.

Regardless of the mechanism, an overall switch from a contractile to an extensile behavior may have relevant implications in tissues. In cell monolayers, cell-substrate forces have been systematically measured to be contractile.[35,36] Transmission of contractility can, in fact, span long distances across monolayers, enabling long-range mechanical force transmission, and downstream effects such as directed migration toward stiff tissues (durotaxis).[36] In such systems, however, forces exerted by cells are only measurable on the substrate, and forces exerted in their mid-plane (where we see extensile forces in our setting) are inaccessible. Potentially, a switch from contractile to extensile behavior induced by cell confinement would dampen overall contractile forces, preventing mechanical force transmission over long distances and ensuing mechanotransduction mechanisms. Such a switch could also be regulated by different factors. One such factor could be dynamic changes in force transmission, such as those that occur during cell division.[37] Another could be substrate stiffness, which strongly affects contractile forces,[20,38] potentially affecting mechanotransduction in stiffening tumors.[39,40] Beyond tumors, a contractile/extensile switch could also affect several other mechanosensitive in vivo processes such as durotaxis in the neural crest,[41] axon growth,[42] sensitivity to long-range force transmission in muscles.[43]

How cells acquire and maintain their shape, how this impacts tissue shape, and the relationship between cell shape and function have been central questions in cell biology.[44–46] To answer them, researchers have developed different techniques. Microcontact printing enabled researchers to decipher the impact of cell spreading area in 2D on cell fate,[47] cellular organization,[48,49] or cell ability to generate forces.[4,5] Microniche systems were later developed to fully control cell shapes in 3D. Made of stiff substrates or structured hydrogels, these microniches can host from a single cell to an organoid and have been used to decipher shape/function relationships for example in hepatocyte doublets,[14] or stem cell colonies.[50] In recent years, they have become widely used, and have also become more refined.[15,50] Our developed system is applicable to such microniche systems, either in single-cell settings as done here or in multicellular settings.

In conclusion, we developed a new system: 3D-µTFM, where we applied 3D-TFM to micro-structured gels to measure previously inaccessible force patterns, which depend on 3D cell morphology. This system can be combined with current microniche technologies, adding a mechanical dimension to the study of cell shape/function relationships in 3D.

4. Experimental Section

Cell Culture: Mammary epithelial cells (MCF10A) were purchased from ATCC and MCF-7 cells were obtained from the van Rheenen laboratory (Netherlands Cancer Institute, The Netherlands). MCF10A cells were used for a maximum of 30 passages and were cultured in Dulbecco's modified Eagle medium DMEM-F12 (LifeTechnologies, 21331–020) with horse serum (5%), penicillin–streptomycin (1%), EGF (20 ng mL^{-1}), hydrocortisone (0.5 µg mL^{-1}), cholera toxin (100 ng mL^{-1}), and insulin (10 µg mL^{-1}). MCF-7 cells were cultured in Dulbecco's modified Eagle medium (DMEM; Gibco, 41966–029) supplemented with heat-inactivated fetal bovine serum (10%, Sigma–Aldrich, 9040–46-8), L-glutamine (2 mM; Gibco; 25030–024) and penicillin–streptomycin (100 U mL^{-1}; Gibco,15070-063). All cells were regularly tested for mycoplasma contamination. When used, blebbistatin (Sigma Aldrich – B0560) was used at a concentration of 25 µM and Latrunculin A (Sigma Aldrich – L5163) at a concentration of 0.5 µM.

Fabrication of Microstructured Polyacrylamide (PAA) Hydrogels: Gels were prepared as described previously.[17] Briefly, PDMS prepolymer (Sylgard 184 Silicon Elastomer, Dow Corning) mixed at a ratio of 10:1 w w^{-1} was spun–coated onto a silicon mold containing wells of 15, 19, or 24 µm of diameter spaced 100 µm from each other, forming thin membranes of 50 µm in thickness. Silicon molds were fabricated on silicon wafers made from SU8-50 using conventional photolithography. PDMS was then cured overnight at 65 °C. After curing, PDMS membranes were cut into pieces including both structured and flat regions, and put onto an 18 mm glass coverslip. 6 well – glass bottom MatTek was used to cast the hydrogels. First, glass silanization was performed to ensure a stable attachment of PAA hydrogels. To this end, glass coverslips were incubated for 15 min with 3-(Trimethoxysilyl)propyl methacrylate (Sigma Aldrich – 440159), acetic acid (Sigma Aldrich – 1612), and 96% ethanol at a ratio of 1:1:14 v/v, rinsed three times with 96% ethanol and dried.

PAA hydrogel mix was prepared as described previously.[19,20] For 15 kPa gels, 19% v/v of acrylamide 40% (Bio-rad – 161-0140) and 8% v/v bis-acrylamide 2% (Bio-rad: 1610142) were added to produce the gels and mixed with 2% v/v fluorescent carboxylated 200 nm beads (Invitrogen), 0.5% v/v APS (Sigma Aldrich – A3678), and 0.05% v/v tetramethyl–ethylene–amine (Sigma Aldrich – T9281). To achieve covalent functionalization of the PAA hydrogels, acrylic acid (Sigma Aldrich – 147230) was added to the mix as a co-monomer of acrylamide and at a 2% concentration of monomers. To cast the gels, a PDMS ring spacer (100–150 um thick) was placed on the glass bottom of the MatTek dishes. 100 µL of gel mix was poured inside the rings and immediately covered by the 18 mm glass coverslip with the PDMS mold thus putting the mold in contact with the PAA hydrogel. PAA hydrogels were left to polymerize for 2 h at room temperature. The polymerized hydrogels were de-molded by carefully removing the coverslip and then stored in PBS for later activation and functionalization.

For 150 kPa gel, 30% v/v of acrylamide 40% (Bio-rad – 161-0140) and 30% v/v bis-acrylamide 2% (Bio-rad: 1610142) were added to produce the gels and mixed with 2% v/v fluorescent carboxylated 200 nm beads (Invitrogen) and 1% v/v Irgacure 2959 (BASF). To achieve covalent functionalization of the PAA hydrogels, acrylic acid (Sigma – 147 230), 0.15% v/v for 15 kPa gels and 0.45% v/v for 15 kPa gels was added. To cast the gels, 15 uL of gel mix was poured on the glass bottom of the MatTek dishes and covered with a 12 mm glass coverslip presenting the pillar patterns in Norland Optical Adhesive 81. PAA hydrogels were polymerized for 15 min under a UV lamp at room temperature. The polymerized hydrogels were de-molded by carefully removing the coverslip and then stored in PBS for later activation and functionalization.

Functionalization of the Structured PAA Hydrogels: First, the acid groups present in the gel were activated through the EDC (1-Ethyl-3 (3′-dimethylaminopropyl) carbodiimide HCL, Merk – 8510070025) NHS (N-Hydroxysuccinimide, Sigma – 130672) chemistry. Briefly, 190 mg of EDC was mixed with 230 mg of NHS and diluted in 10 mL of 20 mM HEPES, pH7 (Life Technologies: 15630056), added to the gel, and incubated at 37 °C for 20 min. The gels were then rinsed once with PBS and incubated with a 30 µg mL^{-1} fibronectin solution (fibronectin from human plasma, F0895 Sigma Aldrich) for 1 h at room temperature. Finally, the gels were rinsed and passivated using a poly(L-lysine) – G – poly(ethylene glycol) (Susos AG: PLL (20 kDa)-g[3,5]-PEG (2) solution at 0.1 mg mL^{-1} in PBS for 1 h at room temperature.

3D Traction Force Microscopy – Imaging: Cells were seeded overnight on structured PAA hydrogels, fabricated as described above. The next morning, cells were labeled using red CellTracker (ThermoFisher Scientific – C34552) diluted at 0.03% v/v in media for 25 min at 37 °C.

Traction force experiments were carried out using the fast-Airyscan mode of an inverted Zeiss LSM880 confocal with a glycerin immersion 40X/1.2 objective equipped with control of temperature, CO_2, and humidity. For each condition, small regions of interest were defined around wells that would present a cell. Only cells completely filling wells, and not spreading or protruding out of the wells, were selected for imaging and subsequent analysis. Additionally, a neighboring region of interest containing an empty well was also analyzed as a control of gel swelling. To obtain 3D images of the wells, stacks were taken with a z-step of 0.2 µm. Fluorescent images of the beads and cells were acquired at the initial time point, after the addition of the drug, and after cell trypsinization (only for the image of the beads).

3D Traction Force Microscopy – Analysis: All codes generated are available at https://github.com/xt-prc-lab/3D_Micropatterned_Traction_Force_Microscopy.git.

3D-PIV: A confocal fluorescence microscopy stack was acquired spanning the whole depth of the well, both when deformed by a cell and after relaxation by trypsin or drugs, with a z-step of the objective (Δs) of 0.2 µm. The axial positional shift of the focal plane (Δf), due to the refraction index mismatch between the sample ($n2$) and the immersion medium of the objective ($n1$), was corrected via Visser's formula.[51]

$$\Delta_f = \frac{\tan(\arcsin(NA/n1))}{\tan(\arcsin(NA/n2))}\,\Delta_s \quad (1)$$

where NA is the numerical aperture of the objective. It is known that Visser's formula might not be quantitatively accurate for some combinations of samples and objectives,[52] thus, its applicability by reconstructing the shape of spherical particles embedded in PAA gels was checked.

The 3D displacement field of the whole gel around the well was calculated by implementing a custom 3D PIV in Matlab (MathWorks, Inc.).[53,54] The whole stack was discretized in individual interrogation boxes, and their relative displacement between the deformed and reference configuration was calculated.

The accuracy of PIV depends on the seeding density of the particles embedded and a high density is desirable for an increase of the signal-to-noise ratio of the measurements. To minimize noise in 2D PIV, the interrogation windows should contain between 4 and 10 particles.[55] For 3D PIV, Bar-Kochba and coworkers,[56] showed, in Figure S1 (Supporting Information), that the error of the 3D PIV decreases with the number of particles in the interrogation boxes, rapidly saturating for densities higher than 0.0005 particles per voxel. For our 32 × 32 × 8 pixel interrogation volumes, this density translates to around four particles per interrogation volume. In our experimental setup, around 12 particles per voxel on the surface of the gel was typically encountered, reducing any error relative to seeding density in our measurements.

The size of the tracing particles also impacts the accuracy of the PIV-measured displacement field (see Figure 5.32 in:[57]), with an optimal diameter of around 2.3 pixels. In our microscopy images, this optimal value translates to around 240 nm. In our experimental setup, fluorescent beads with a nominal diameter of 200 nm, close to the optimal value were used.

Traction Inference Using Finite Element Modelling: A direct approach is first considered, in which the measured 3D displacement field on the surface of the gel (top surface and well surface) was imposed as boundary conditions in a finite element model of the well. This approach was implemented in Matlab (MathWorks) and Abaqus (Dassault Systemes). Geometrically, a square prism was considered with the same height as the gel with a cylindrical cavity on the top surface of the same depth and average radius as the physical well. The edges of the cylinder were rounded

using a radius of 0.5 µm for the bottom edge and of 1 µm for the top edge of the cylinder to closely follow the geometry of the physical wells. Each model was meshed in Abaqus with hybrid 4-node linear tetrahedron elements. The gel as a hyperelastic solid to account for possible geometrical and material nonlinearities was modeled. The geometry of the mesh was imported in Matlab, and the 3D displacement values of each node at the surface of the gel were interpolated from the 3D PIV displacement field. This approach, however, resulted in non-zero tractions at the top surface of the gel, although this part of the surface did not interact with cells. Imposing the 3D displacement only at the well surface fixes this issue but disregards experimental measurements at the top surface. To use all measured data while obtaining mechanically meaningful results consistent with force balance, an inverse approach was developed as detailed in Note S1 (Supporting Information).

Unfolding of the Deformation and Traction Fields: The deformation field measured by the PIV was provided in a 3D volume around the well, without information on the location of the different surfaces of our system. To locate the upper surface of the gel, the mean intensity of each plane of the fluorescent bead microscopy image stack was calculated. The peak location of this distribution provided the plane of the gel's surface. Any consistent signature on the mean intensity signal pointing toward the location of the base of the well was not found. If using the standard deviation of the intensity rather than the mean, the largest peak also indicated the location of the upper surface, while the second peak pointed toward the general location of the well's bottom. However, this second peak contained too many errors in our measurements to be used. The bottom of the well with an offset, equal to the model's depth, from the upper surface of the gel was located. To locate the surface of the vertical wall of the well, it is first detected the well circumference in a central plane, either automatically or manually, and then its center. The wall surface was then defined as a cylinder with the same radius as the well.

Given the regular shapes of the mesh of the model of the wells, the location of the different surfaces was readily available for the traction fields. The upper surface of the gel was composed of the nodes with the highest z-coordinate. The bottom surface of the well was composed of the nodes with the lowest z-coordinate, and the rest belonged to the wall of the well. It is important to notice that the nodes at the rounded area between the upper surface of the gel and the vertical wall of the well are where the highest discretization errors and geometrical uncertainties were present. With this in mind, the upper rounded area (around 1 µm) from the wall of the well region in the unfolded maps was excluded. The traction maps so defined are composed of discrete points (the nodes of the model). To provide a continuous representation, the maps with Matlab's 2D interpolation of scattered data, *scatteredInterpolant*, with the *natural neighbor interpolation* method were interpolated.

Immunostaining: For immunostaining, the cells were fixed with paraformaldehyde (4%) for 10 min. Permeabilization and blocking were done in one step with TritonX-100 (0,1%, Sigma T8787) and fish gelatin (0.5%, Sigma G7765) in PBS for 30 min. Cells were incubated with 1/1000 phalloidin-Atto 488 (Sigma–Aldrich, category no. 49409) in fish gelatin (0.5%) for 1 h at room temperature. Hoechst 33258 staining dye was used for nuclear labeling following 10 min incubation at room temperature. Finally, cells were imaged in PBS no more than 24 h after the end of the staining step.

Immunostaining Imaging: Immunofluorescence images were performed in a Nikon TiE inverted microscope with a spinning-disc confocal unit (CSU-WD, Yokogawa) and a Zyla scientific complementary metal–oxide–semiconductor camera (Andor) with µManager (version 1.4.22), using a ×60 objective (Plan Apo; numerical aperture (NA), 1.2; water-immersion type) and with a ZEISS LSM 880 inverted confocal microscope with Airyscan and a ×40 1.456-NA glycerin-immersion objective and ZEN (ZEISS, version 2.3 SP1 FP3 black) software. To obtain 3D images of the wells, stacks were taken with a z-step of 0.2 µm.

Actin Quantification: All steps were performed using FIJI software. Immunofluorescence stacks were recut to 250×250 px around the well in xy; in z, only the planes presenting actin fluorescence were kept. Cell volume was approximated by a cylinder, with a diameter measured through the actin cortex staining in the well, and a height measured through the number of planes kept for the analysis. To measure the actin amount in the stacks the background was subtracted and the integrated fluorescence intensity in all slices was calculated (RawIntDen in FIJI). RawIntDen was used as a measure of the actin amount for each cell. Finally, data were normalized using the mean of the RawIntDen for each day. In total, $n = 12$ cells coming from three independent experiments were analyzed.

Statistical Analysis and Graphic Representation: In the T_n-wall, T_v-wall, and T_c-wall profile representations, as some profiles were longer than others (12 µm deep wells compared to 11 µm deep wells, for example) all profiles were aligned to the same lowest point. The same was done for the representation of the normal displacement to the wall of the well. Finally, when aligned, if only one profile was longer than the other, the extra values were not displayed as they were not associated with any standard deviation.

Statistical analyses were performed using GraphPad Prism software (version 8). Statistical significance was determined by the specific tests indicated in the corresponding figure legends. Non-parametric tests were performed when neither original nor log-10-transformed datasets were normally distributed. All the experiments presented here were repeated in at least three independent experiments. The number of cells analyzed is specified for each experiment in the figure legends.

Code Availability: All generated codes are available at https://github.com/xt-prc-lab/3D_Micropatterned_Traction_Force_Microscopy.git.

Supporting Information

Supporting Information is available from the Wiley Online Library or from the author.

Acknowledgements

L.M.F., and M.G.-G. contributed equally to this work. The authors thank A. Del campo for initial discussion, S. Usieto, A. Menéndez, N. Castro, M. Purciolas, M Morcillo Sanchez, and E. Coderch Bifet for providing technical support; E. Latorre, I. Granero-Moya and M. Matejcic for providing data analysis tools; E. Dalaka for her AFM expertise, JB. Fiche, Z. Kechagia, A. Labernadie, A Beedle, A.L. Le Roux, L. Rosetti, R. Sunyer, and V. Venturini as well as all the members of the groups of P.R.-C. and X.T. for helpful discussions. The authors acknowledge funding from the EMBO organization (Postdoctoral fellowship ALTF 2–2018), the Spanish Ministry of Science and Innovation (PID2021-128635NB-I00 MCIN/AEI/10.13039/501100011033 and "ERDF-EU A way of making Europe" to X.T., PID2019-110949GB-I00 to M.A., PID2022-142672NB-I00 to P.R.-C. and PID2021-129115OB-I00), the European Commission (H2020-FETPROACT-01-2016-731957), the European Research Council (Adv-883739 to X.T.; CoG-681434 to M.A.; grant 101097753 MechanoSynth to P.R-C), the Generalitat de Catalunya (2017-SGR-1602 to X.T. and P.R.-C.; 2017-SGR-1278 to M.A.), European Union's Horizon 2020 research and innovation program under the Marie Skłodowska-Curie grant agreement no. 797621 to M.G.-G., The prize "ICREA Academia" for excellence in research to M.A. and P.R.-C., Fundació la Marató de TV3 (201936-30-31 and 201903-30-31-32), and "la Caixa" Foundation (LCF/PR/HR20/52400004 and ID 100010434 under agreement LCF/PR/HR20/52400004). IBEC and CIMNE are recipients of a Severo Ochoa Award of Excellence from MINCIN.

Conflict of Interest

The authors declare no conflict of interest.

Data Availability Statement

The data that support the findings of this study are available in the supplementary material of this article.

Keywords

cell volumes, cytoskeleton, micro-wells, traction forces

Received: June 21, 2024
Revised: September 20, 2024
Published online: October 23, 2024

[1] L. Rhumbler, *Archiv. für. Entwicklungsmechanik. der Organismen.* **1902**, *14*, 401.
[2] P. E. Young, T. C. Pesacreta, D. P. Kiehart, *Development.* **1991**, *111*, 1.
[3] M.-C. Diaz-de-la-Loza, R. P. Ray, P. S. Ganguly, S. Alt, J. R. Davis, A. Hoppe, N. Tapon, G. Salbreux, B. J. Thompson, *Dev. Cell.* **2018**, *46*, 23.
[4] P. Roca-Cusachs, J. Alcaraz, R. Sunyer, J. Samitier, R. Farré, D. Navajas, *Biophys. J.* **2008**, *94*, 4984.
[5] A. J. Ribeiro, Y.-S. Ang, J.-D. Fu, R. N. Rivas, T. M. Mohamed, G. C. Higgs, D. Srivastava, B. L. Pruitt, *Proc. Natl. Acad. Sci. U.S.A.* **2015**, *112*, 12705.
[6] R. Kumar, S. Saha, B. Sinha, *Biochimica et Biophysica Acta (BBA) – Molecular Cell Res.* **2019**, *1866*, 118516.
[7] J. L. Tan, J. Tien, D. M. Pirone, D. S. Gray, K. Bhadriraju, C. S. Chen, *Proc. Natl. Acad. Sci. U.S.A.* **2003**, *100*, 1484.
[8] S. A. Maskarinec, C. Franck, D. A. Tirrell, G. Ravichandran, *Proc. Natl. Acad. Sci. U.S.A.* **2009**, *106*, 22108.
[9] C. Franck, S. A. Maskarinec, D. A. Tirrell, G. Ravichandran, *PLoS One.* **2011**, *6*, e17833.
[10] C. Pérez-González, G. Ceada, F. Greco, M. Matejčić, M. Gómez-González, N. Castro, A. Menendez, S. Kale, D. Krndija, A. G. Clark, V. R. Gannavarapu, A. Álvarez-Varela, P. Roca-Cusachs, E. Batlle, D. M. Vignjevic, M. Arroyo, X. Trepat, *Nat. Cell Biol.* **2021**, *23*, 745.
[11] W. R. Legant, J. S. Miller, B. L. Blakely, D. M. Cohen, G. M. Genin, C. S. Chen, *Nat. Methods.* **2010**, *7*, 969.
[12] J. Steinwachs, C. Metzner, K. Skodzek, N. Lang, I. Thievessen, C. Mark, S. Münster, K. E. Aifantis, B. Fabry, *Nat. Methods.* **2016**, *13*, 171.
[13] J. Barrasa-Fano, A. Shapeti, J. De Jong, A. Ranga, J. A. Sanz-Herrera, H. Van Oosterwyck, *Acta Biomater.* **2021**, *126*, 326.
[14] Q. Li, Y. Zhang, P. Pluchon, J. Robens, K. Herr, M. Mercade, J.-P. Thiery, H. Yu, V. Viasnoff, *Nat. Cell Biol.* **2016**, *18*, 311.
[15] Y. Zhang, R. De Mets, C. Monzel, V. Acharya, P. Toh, J. F. L. Chin, N. Van Hul, I. C. Ng, H. Yu, S. S. Ng, S. Tamir Rashid, V. Viasnoff, *Nat. Mater.* **2020**, *19*, 1026.
[16] M. Bao, J. Xie, A. Piruska, W. T. Huck, *Nat. Commun.* **2017**, *8*, 1962.
[17] J. Comelles, V. Fernández-Majada, N. Berlanga-Navarro, V. Acevedo, K. Paszkowska, E. Martínez, *Biofabrication.* **2020**, *12*, 025023.
[18] M. Dembo, Y.-L. Wang, *Biophys. J.* **1999**, *76*, 2307.
[19] A. Elosegui-Artola, E. Bazellières, M. D. Allen, I. Andreu, R. Oria, R. Sunyer, J. J. Gomm, J. F. Marshall, J. L. Jones, X. Trepat, P. Roca-Cusachs, *Nature Mater.* **2014**, *13*, 631.
[20] Z. Kechagia, P. Sáez, M. Gómez-González, B. Canales, S. Viswanadha, M. Zamarbide, I. Andreu, T. Koorman, A. E. Beedle, A. Elosegui-Artola, P. W. Derksen, X. Trepat, M. Arroyo, P. Roca-Cusachs, *Nat. Mater.* **2023**, *22*, 1409.
[21] R. Rodrigues De Mercado, H. Van Hoorn, M. De Valois, C. Backendorf, J. Eckert, T. Schmidt, *Biomed. Opt. Express.* **2022**, *13*, 464.
[22] S. KWON, S. J. HAN, K. S. KIM, *Oncol. Rep.* **2023**, *50*, 200.
[23] S. Hervas-Raluy, M. J. Gomez-Benito, C. Borau-Zamora, M. Cóndor, J. M. Garcia-Aznar, *PLoS One.* **2021**, *16*, e0249018.
[24] M. Prass, K. Jacobson, A. Mogilner, M. Radmacher, *J. Cell Biol.* **2006**, *174*, 767.
[25] F. Kage, M. Winterhoff, V. Dimchev, J. Mueller, T. Thalheim, A. Freise, S. Brühmann, J. Kollasser, J. Block, G. Dimchev, M. Geyer, H.-J. Schnittler, C. Brakebusch, T. E. B. Stradal, M.-F. Carlier, M. Sixt, J. Käs, J. Faix, K. Rottner, *Nat. Commun.* **2017**, *8*, 14832.
[26] A. Proag, A. Bouissou, T. Mangeat, R. Voituriez, P. Delobelle, C. Thibault, C. Vieu, I. Maridonneau-Parini, R. Poincloux, *ACS Nano.* **2015**, *9*, 3800.
[27] A. Labernadie, A. Bouissou, P. Delobelle, S. Balor, R. Voituriez, A. Proag, I. Fourquaux, C. Thibault, C. Vieu, R. Poincloux, G. M. Charrière, I. Maridonneau-Parini, *Nat. Commun.* **2014**, *5*, 5343.
[28] K. Adebowale, B. Ha, A. Saraswathibhatla, D. Indana, M. C. Popescu, S. Demirdjian, J. Yang, M. C. Bassik, C. Franck, P. L. Bollyky, O. Chaudhuri, *bioRxiv* **2023**, https://doi.org/10.1101/2023.06.09.544394.
[29] P. Chugh, A. G. Clark, M. B. Smith, D. A. D. Cassani, K. Dierkes, A. Ragab, P. P. Roux, G. Charras, G. Salbreux, E. K. Paluch, *Nat. Cell Biol.* **2017**, *19*, 689.
[30] P. Bieling, T.-D. Li, J. Weichsel, R. McGorty, P. Jreij, B. Huang, D. A. Fletcher, R. D. Mullins, *Cell.* **2016**, *164*, 115.
[31] C. G. Muresan, Z. G. Sun, V. Yadav, A. P. Tabatabai, L. Lanier, J. H. Kim, T. Kim, M. P. Murrell, *Nat. Commun.* **2022**, *13*, 7008.
[32] B. A. Truong Quang, R. Peters, D. A. D. Cassani, P. Chugh, A. G. Clark, M. Agnew, G. Charras, E. K. Paluch, *Nat. Commun.* **2021**, *12*, 6511.
[33] A. Biswas, O. Muñoz, K. Kim, C. Hoege, B. M. Lorton, D. Shechter, J. Guck, V. Zaburdaev, S. Reber, *bioRxiv* **2023**, https://doi.org/10.1101/2023.09.05.556409.
[34] Y. Li, K. Konstantopoulos, R. Zhao, Y. Mori, S. X. Sun, *J. Cell Sci.* **2020**, *133*, jcs240341.
[35] R. Vincent, E. Bazellières, C. Pérez-González, M. Uroz, X. Serra-Picamal, X. Trepat, *Phys. Rev. Lett.* **2015**, *115*, 248103.
[36] R. Sunyer, V. Conte, J. Escribano, A. Elosegui-Artola, A. Labernadie, L. Valon, D. Navajas, J. M. García-Aznar, J. J. Muñoz, P. Roca-Cusachs, X. Trepat, *Science.* **2016**, *353*, 1157.
[37] N. Taneja, L. Rathbun, H. Hehnly, D. T. Burnette, *Curr. Opin. Cell Biol.* **2019**, *56*, 45.
[38] A. Elosegui-Artola, R. Oria, Y. Chen, A. Kosmalska, C. Pérez-González, N. Castro, C. Zhu, X. Trepat, P. Roca-Cusachs, *Nat. Cell Biol.* **2016**, *18*, 540.
[39] K. R. Levental, H. Yu, L. Kass, J. N. Lakins, M. Egeblad, J. T. Erler, S. F. Fong, K. Csiszar, A. Giaccia, W. Weninger, M. Yamauchi, D. L. Gasser, V. M. Weaver, *Cell.* **2009**, *139*, 891.
[40] T. Panciera, A. Citron, D. Di Biagio, G. Battilana, A. Gandin, S. Giulitti, M. Forcato, S. Bicciato, V. Panzetta, S. Fusco, L. Azzolin, A. Totaro, A. P. Dei Tos, M. Fassan, V. Vindigni, F. Bassetto, A. Rosato, G. Brusatin, M. Cordenonsi, S. Piccolo, *Nat. Mater.* **2020**, *19*, 797.
[41] A. Shellard, R. Mayor, *Nature.* **2021**, *600*, 690.
[42] D. E. Koser, A. J. Thompson, S. K. Foster, A. Dwivedy, E. K. Pillai, G. K. Sheridan, H. Svoboda, M. Viana, L. D. F. Costa, J. Guck, C. E. Holt, K. Franze, *Nat. Neurosci.* **2016**, *19*, 1592.
[43] T. Finni, H. de Brito Fontana, H. Maas, *J. Biomech.* **2023**, *152*, 111575.
[44] R. Singhvi, A. Kumar, G. P. Lopez, G. N. Stephanopoulos, D. I. Wang, G. M. Whitesides, D. E. Ingber, *Science, New Series.* **1994**, *264*, 696.
[45] T. Lecuit, P.-F. Lenne, *Nat. Rev. Mol. Cell Biol.* **2007**, *8*, 633.
[46] A. Haupt, N. Minc, *J. Cell Sci.* **2018**, *131*, jcs214015.
[47] C. S. Chen, M. Mrksich, S. Huang, G. M. Whitesides, D. E. Ingber, *Science.* **1997**, *276*, 1425.
[48] K. Mandal, A. Asnacios, B. Goud, J.-B. Manneville, *Proc. Natl. Acad. Sci. U.S.A.* **2016**, *113*, E7159.
[49] T. C. Von Erlach, S. Bertazzo, M. A. Wozniak, C.-M. Horejs, S. A. Maynard, S. Attwood, B. K. Robinson, H. Autefage, C. Kallepitis, A.

Del Río Hernández, C. S. Chen, S. Goldoni, M. M. Stevens, *Nature Mater.* **2018**, *17*, 237.
[50] M. Bao, J. Xie, *ACS Appl. Mater Interfaces* **2023**, *15*, 34397.
[51] T. D. Visser, J. L. Oud, G. J. Brakenhoff, *Optik.* **1992**, *90*, 17.
[52] E. E. Diel, J. W. Lichtman, D. S. Richardson, *Nat. Protoc.* **2020**, *15*, 2773.
[53] J. Barbazan, C. Pérez-González, M. Gómez-González, M. Dedenon, S. Richon, E. Latorre, M. Serra, P. Mariani, S. Descroix, P. Sens, X. Trepat, D. M. Vignjevic, *Nat. Commun.* **2023**, *14*, 6966.
[54] E. Latorre, S. Kale, L. Casares, M. Gómez-González, M. Uroz, L. Valon, R. V. Nair, E. Garreta, N. Montserrat, A. Del Campo, B. Ladoux, M. Arroyo, X. Trepat, *Nature.* **2018**, *563*, 203.
[55] R. Theunissen, F. Scarano, M. L. Riethmuller, *Meas. Sci. Technol.* **2007**, *18*, 275.
[56] E. Bar-Kochba, J. Toyjanova, E. Andrews, K.-S. Kim, C. Franck, *Exp Mech.* **2015**, *55*, 261.
[57] M. Raffel, C. E. Willert, F. Scarano, C. J. Kähler, S. T. Wereley, J. Kompenhans, *Particle Image Velocimetry*, Springer, Berlin **2018**.